Article

A First-Principles Calculation Study of the Catalytic Properties of Two-Dimensional Bismuthene Materials for Carbon Dioxide Reduction

Chang-Tian Wang [1,†] , Qinchi Yue [2,†], Changhao Wang [2] , Yuanji Xu [3] and Chang Zhou [4,*]

1 Beijing Advanced Innovation Center for Materials Genome Engineering, Department of Physical Chemistry, University of Science and Technology Beijing, Beijing 100083, China; ctwang@ustb.edu.cn
2 Key Laboratory of Advanced Functional Materials of Education Ministry of China, College of Materials Science and Engineering, Beijing University of Technology, Beijing 100124, China; yueqinchiy@163.com (Q.Y.); wangch33@bjut.edu.cn (C.W.)
3 Institute for Applied Physics, University of Science and Technology Beijing, Beijing 100083, China; yuanjixu@ustb.edu.cn
4 State Key Laboratory for Advanced Metals and Materials, University of Science and Technology Beijing, Beijing 100083, China
* Correspondence: changzhou@ustb.edu.cn
† These authors contributed equally to this work.

Abstract: The electrochemical reduction of carbon dioxide (CO_2) at room temperature into industrial chemicals and energy products offers a promising strategy to mitigate atmospheric greenhouse gas emissions. In this study, bismuthene was employed as a catalyst for CO_2 reduction reaction (CO_2RR). Through first-principles calculations, we evaluated the CO_2RR catalytic activities of bismuth (Bi) on the (001) and (012) surfaces, analyzing the mechanisms underlying these activities. Surface energy calculations for monolayer and multilayer bismuthene confirmed that monolayer bismuthene is stable and suitable for catalytic applications. Adsorption free energies of intermediates showed that formic acid is the primary product. Furthermore, it is found that the Bi(012) surface has a lower free energy barrier than Bi(001) in the CO_2RR process, representing the higher catalytic activity. These results provide theoretical insights for designing bismuthene-based CO_2RR catalysts with reduced overpotential, improved efficiency and enhanced selectivity, particularly enhancing catalyst selectivity.

Keywords: bismuthene; 2D materials; first-principles calculations; carbon dioxide (CO_2); catalyze

1. Introduction

Since Geim et al. successfully exfoliated single-layer graphene using adhesive tape in 2004 [1], the intriguing electronic properties of graphene have ignited intense interest in layered two-dimensional (2D) materials. As research into 2D materials has advanced, researchers have discovered that these materials exhibit numerous exciting novel properties, such as larger bandgaps and tunable electronic, optoelectronic, catalytic, and photoelectrochemical properties, compared to their bulk counterparts [2–7]. Thus, 2D materials are set to be a key foundation for future advances in electronics, optoelectronics, energy conversion, and storage. Research on CO_2 catalytic reduction supports a sustainable carbon cycle, helping to reduce the greenhouse effect and tackle the energy crisis [8].

Two-dimensional electrocatalysts enriched with nanostructures represent a common and effective approach to enhancing catalytic performance. Due to their larger specific sur-

face area, 2D electrocatalysts, particularly those with abundant edge structures containing unsaturated sites [9], provide significantly more active catalytic sites compared to bulk materials. Bismuth (Bi), characterized by higher-order topological properties, is classified as a higher-order topological insulator (HOTI). The bulk–boundary correspondence under time-reversal symmetry protection [10] suggests that these unique physicochemical properties endow low-dimensional Bi metallic catalysts with unparalleled catalytic performance compared to their bulk counterparts. Theoretically, it is predicted that one to eight bismuth (111) bilayers form a 2D topological insulator, while films exceeding eight bismuth (111) bilayers in thickness transition into a topologically trivial phase [11]. Bismuthene is a material formed by a single layer of bismuth atoms arranged in a two-dimensional honeycomb structure.

Among the products of the CO_2 reduction reaction (CO_2RR) are compounds such as CO, CH_4, C_2H_4, HCOOH, and C_2H_5OH. Several electron and proton transfer processes are involved. CO_2 can be reduced to a range of gaseous and liquid products through various pathways, including hydrocarbons (such as CH_4 and C_2H_4), alcohols (such as CH_3OH and C_2H_5OH), carbon monoxide (CO), and formic acid (HCOOH) [12–15]. The intermediates of multi-electron transfer reactions are numerous [16–18], and the reduction process is complex [19,20], leading to suboptimal utilization of electrical energy and low Faradaic efficiency [21,22]. Moreover, due to the high overpotential required for the activation of CO_2 molecules, transferring an electron from CO_2 requires a potential more negative than -1.90 V (relative to the standard hydrogen electrode (SHE)) [23]. Sliwa et al. developed a scalable, room-temperature method for synthesizing homogeneous AgCu alloy nanoparticles with tunable Cu content, achieving high efficiency and selectivity in CO_2 reduction at mild overpotentials, making them highly effective for electrocatalysis [24]. Experiments conducted by Sun et al. have confirmed the topological nature of 2D bismuth (111) films on $NbSe_2$ substrates [25]. Bismuthene has demonstrated excellent catalytic activity and high product selectivity in electrochemical CO_2 reduction [26–33], making it highly promising for CO_2 reduction reaction (CO_2RR) catalysis. For the Bi(001) surface, recent studies have reported the related experimental and theoretical work. Siinor et al. studied the application of the Bi(001) single-crystal plane electrode to impedance spectroscopy [34]. Bi(001) is also used as a substrate in grown rubrene monolayers [35].

This study employs density functional theory to investigate the potential of bismuthene as a catalyst for CO_2 reduction. We analyzed the structural stability of bismuthene with varying numbers of layers by calculating the surface energy while considering spin–orbit coupling (SOC) [36]. The results confirmed that monolayer bismuthene has the lowest surface energy, indicating superior stability. By calculating the surface adsorption free energies of various intermediates involved in CO_2RR on the monolayer Bi(001) and Bi(012) surfaces, we constructed potential diagrams, which demonstrated that formic acid is the catalytic product of CO_2RR and that the Bi(012) surface exhibits higher catalytic activity compared to the Bi(001) surface. We find that this catalyst exhibits a reaction advantage for CO_2RR over the hydrogen evolution reaction (HER). Electronic band structures reveal that different intermediates have distinct effects on the electronic properties of the systems, providing an explanation for their catalytic activity from the perspective of electronic band theory. This work provides valuable theoretical insights for designing bismuthene-based CO_2RR catalysts with desirable properties, including lower overpotential, higher selectivity, and enhanced catalytic efficiency.

2. Computational Method and Materials

The first-principles calculations are based on the density functional theory (DFT) as implemented in the Vienna ab initio simulation package (VASP) [37,38]. To model

the interaction between ionic cores and valence electrons, the projector-augmented-wave (PAW) method [39,40] was used, with valence electrons employed as $6s^2p^3$ for Bi, $2s^2p^2$ for C, $2s^2p^4$ for O, and $1s^1$ for H. The exchange-correlation interactions are considered in the generalized gradient approximation (GGA) using the Perdew–Burke–Ernzerhof (PBE) functional [41,42]. A plane-wave basis set with an energy cutoff of 550 eV is used. The calculations were also performed with the DFT-D3 methods developed by Grimme et al., which consider the dispersion correction and adds the Van der Waals interaction to the conventional Kohn–Sham DFT potential energy [43,44]. The spin–orbit coupling (SOC) effect is considered in calculations [36].

The bulk Bi structure is shown in the upper part of Figure 1a, which has a 6-atom hexagonal unit cell in $R\bar{3}m$ (166) symmetry with lattice parameters a = b = 4.63 Å and c = 12.25 Å, and the Bi atoms occupy the 6c (0, 0, 0.2674) Wyckoff position. The Bi(001) and Bi(012) surfaces are constructed by cleaving the bulk Bi structure, with a 15 Å vacuum layer along the Z direction, and are named as the Bi-001-i-Layer and Bi-012-i-Layer, respectively. The Bi-001-1-Layer is modeled by a periodic one-layer 4×4 slab. The lattice constants of the Bi-001-1-Layer are a = 18.54 Å, b = 18.54 Å, and c = 16.61 Å, respectively. The Bi-012-1-Layer is modeled by a periodic 1-layer 3×3 slab. The lattice constants of the Bi-012-1-Layer are a = 13.90 Å, b = 14.65 Å, and c = 15.23 Å. The structures of bismuthene are optimized with the convergence criteria for the electronic self-consistent relaxation and the ionic relaxation set to 10^{-6} eV and 10^{-2} eV/Å for energy and force, respectively. The Brillouin zone is sampled with a $3 \times 3 \times 1$ Γ-centered Monkhorst–Pack k-point grid.
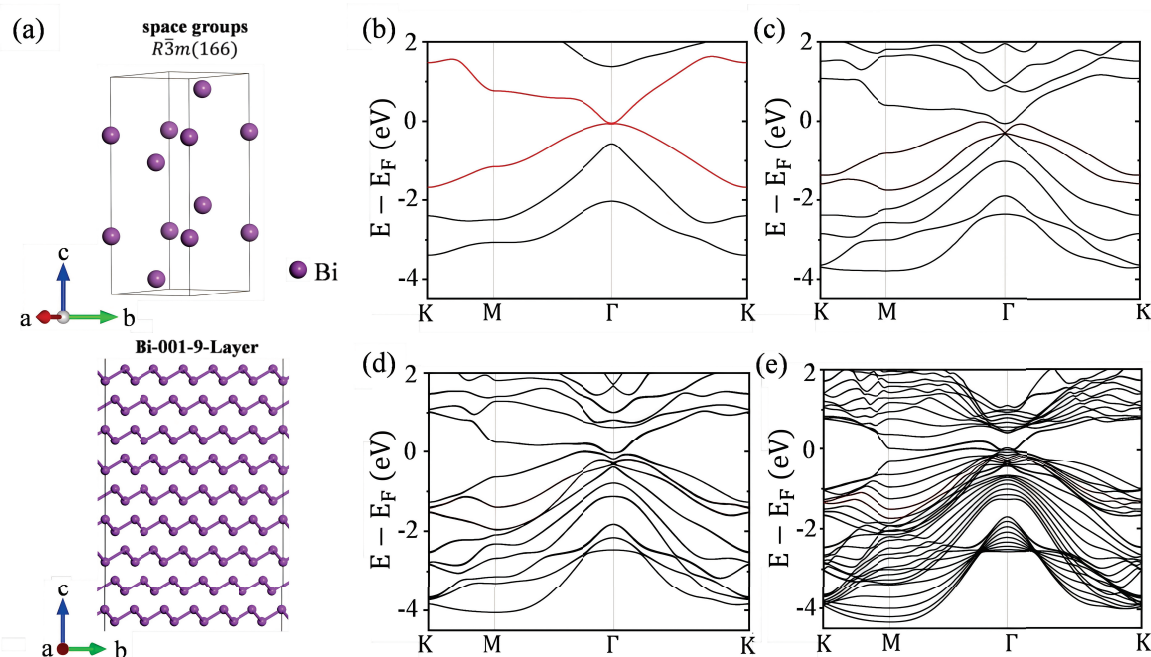

Figure 1. (**a**) The upper part illustrates the primitive cell of the bulk Bi structure, while the lower part shows the Bi-001-9-Layer. The band structures of the Bi-001-i-Layer without SOC are presented in (**b**–**e**) for i = 1, 2, 3, 9, respectively. The red lines in (**b**) represent the surface states of the 1-layer Bi(001) surface.

3. Results and Discussion

3.1. Surface Energy and Band Structures of Bismuthene

Bismuth (Bi), belonging to the space group $R\bar{3}m$ (166) and possessing time-reversal symmetry, is illustrated in the upper part of Figure 1a. It exhibits bulk–boundary correspondence under time-reversal symmetry protection. The unique physicochemical properties

endow low-dimensional Bi metal catalysts with unparalleled catalytic performance compared to their bulk counterparts. The lower part of Figure 1a shows the Bi-001-9-Layer. The surface energy of few-layer bismuthene is calculated using the Equation (1) below:

$$E_{\text{surface}} = \frac{1}{2S}(E_{\text{Bi-iL}} - n \cdot E_{\text{Bi}}), \tag{1}$$

where E_{surface} represents the surface energy of the 2D material; $E_{\text{Bi-iL}}$ denotes the energy of the *i*-layer bismuthene; E_{Bi} refers to the energy of a single atom in bulk Bi; *n* is the number of atoms in the unit cell of the *i*-layer bismuthene; and *S* is the surface area of the bismuthene. The surface energies of the Bi-001-1-layer, Bi-001-2-layer, Bi-001-3-layer, and Bi-001-9-layer bismuthene structures are 0.0088 eV·Å^{-2}, 0.0098 eV·Å^{-2}, 0.0102 eV·Å^{-2}, and 0.0105 eV·Å^{-2}, respectively. Surface energy analysis reveals that bismuthene structures with fewer layers exhibit lower surface energy and greater stability. As a result, monolayer bismuthene is more stable compared to multilayer structures. This computational result has also been experimentally validated, as monolayer Bi can be synthesized in the laboratory [45,46].

Band structure analysis shows a significant band overlap at the Fermi level in the band diagram of the Bi-001-1-Layer (Figure 1b), with the surface states indicated by red lines. The calculated results show that the valence and conduction bands of Bi-001-1-Layer intersect at the Γ-point on the Fermi level. As the number of Bi atomic layers increases, there is a slight increase in the number of bands near the Fermi surface, as shown in Figure 1c–e. As the film thickness increases (when the thickness is approximately above 34 Å), these bands will merge into a continuum in the bulk limit.

3.2. Free Energy Analysis of Intermediates in Bismuthene for CO_2RR

DFT calculations were utilized to investigate the free energy of three reaction pathways on the Bi-001-1-Layer and Bi-012-1-Layer,

1. *OCO ⟶ *OCHO;
2. *OCO ⟶ *COOH;
3. *H ⟶ H_2.

Figure 2 presents a detailed illustration of the two potential reaction pathways for CO_2RR. Based on thermodynamic data, the energy change for the formic acid production pathway in CO_2RR was calculated to be 0.331 eV [47]. Since the complete reaction process involves two electron transfer steps, such as the formation of *COOH and formic acid, the average energy per step is 0.1655 eV.

Table 1 lists the calculation results of reaction Gibbs free energies (G) of various intermediates in the CO_2RR and the changes in Gibbs free energy (ΔG) at U = 0 V versus RHE and U = 0.1655 V versus RHE. The results of U = 0.1655 V versus RHE are represented in Figure 3. A comparison of Figure 3a,b reveals that calculations excluding SOC may overestimate the adsorption energy during the CO_2RR process. The ΔG of the conversion of adsorbed CO_2 molecules to *OCOH on Bi(001) and Bi(012) is 0.8303 eV and 0.654 eV, respectively. The ΔG of the conversion of adsorbed CO_2 molecules to *COOH on Bi(001) and Bi(012) is 1.432 eV and 0.722 eV, respectively. It is observed that the free energy required for the conversion of adsorbed CO_2 molecules to *COOH is greater than that for the conversion to *OCHO on both the Bi(001) and Bi(012) surface. This suggests that both the Bi(001) and Bi(012) active surfaces have high selectivity for the formation of *OCHO,the only catalytic product of the intermediate is formic acid, leading to the conclusion that the catalytic products of CO_2RR on these substrates are formic acid. Moreover, bismuthene and Bi nanosheets have been experimentally confirmed to exhibit high electrocatalytic efficiency for formate (*OCOH) formation from CO_2 reduction, with a Faradaic efficiency

of 99% at −0.58 V vs. Reversible Hydrogen Electrode (RHE) for bismuthene and a Faradaic efficiency of 94.5% at −0.98 V vs. RHE for 1.5 nm Bi nanosheets [33,48].
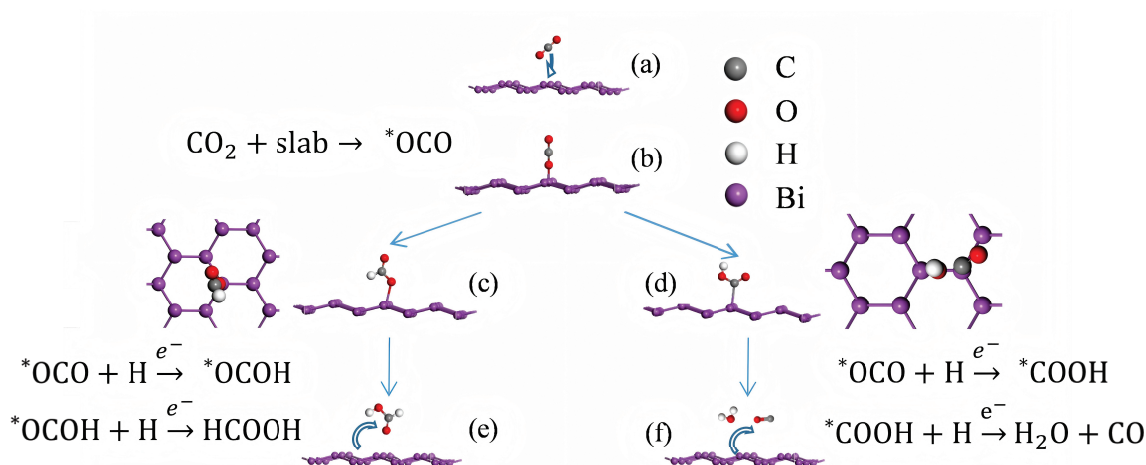

Figure 2. Degradation pathways of CO_2 on the catalyst surface by first-principles calculations. (**a**) CO_2 molecule adsorption, (**b**) *OCO adsorbed intermediate formation, (**c**) *OCOH adsorbed intermediate formation, (**d**) *COOH adsorbed intermediate formation, (**e**) formic acid molecule desorption from the catalyst surface, and (**f**) carbon monoxide and water molecule desorption from the catalyst surface.

Furthermore, the rate-determining step (RDS) of CO_2RR on the (012) surface is the adsorption of *OCO with the ΔG of 0.654 eV (Figure 3c). And the RDS of (001) surface is the reaction of *OCO to *OCOH with the ΔG of 0.830 eV (Figure 3a). The lower RDS on (012) surface indicates that the Bi-012-1-Layer has higher catalytic efficiency than the Bi-001-1-Layer.

Table 1. Reaction free energies (G) of various intermediates in the CO_2RR on different exposed surfaces of Bi-1-Layer, as well as the changes in free energy at applied potentials of U = 0 V versus RHE and U = 0.1655 V versus RHE (vibrationally corrected).

Absorb Structure	G/eV	ΔG/eV (U = 0 V)	ΔG/eV (U = 0.1655 V)
		Bi-SOC-001-1-Layer	
slab	−167.247	0.000	0.000
*OCO	−166.833	0.414	0.414
*OCOH	−165.837	1.410	1.244
*slab	−166.916	0.331	0.000
*COOH	−165.235	2.012	1.846
		Bi-nonSOC-001-1-Layer	
slab	−148.332	0.000	0.000
*OCO	−147.447	0.885	0.885
*OCOH	−146.727	1.605	1.439
*slab	−148.001	0.331	0.000
*COOH	−146.359	1.973	1.851

Table 1. *Cont.*

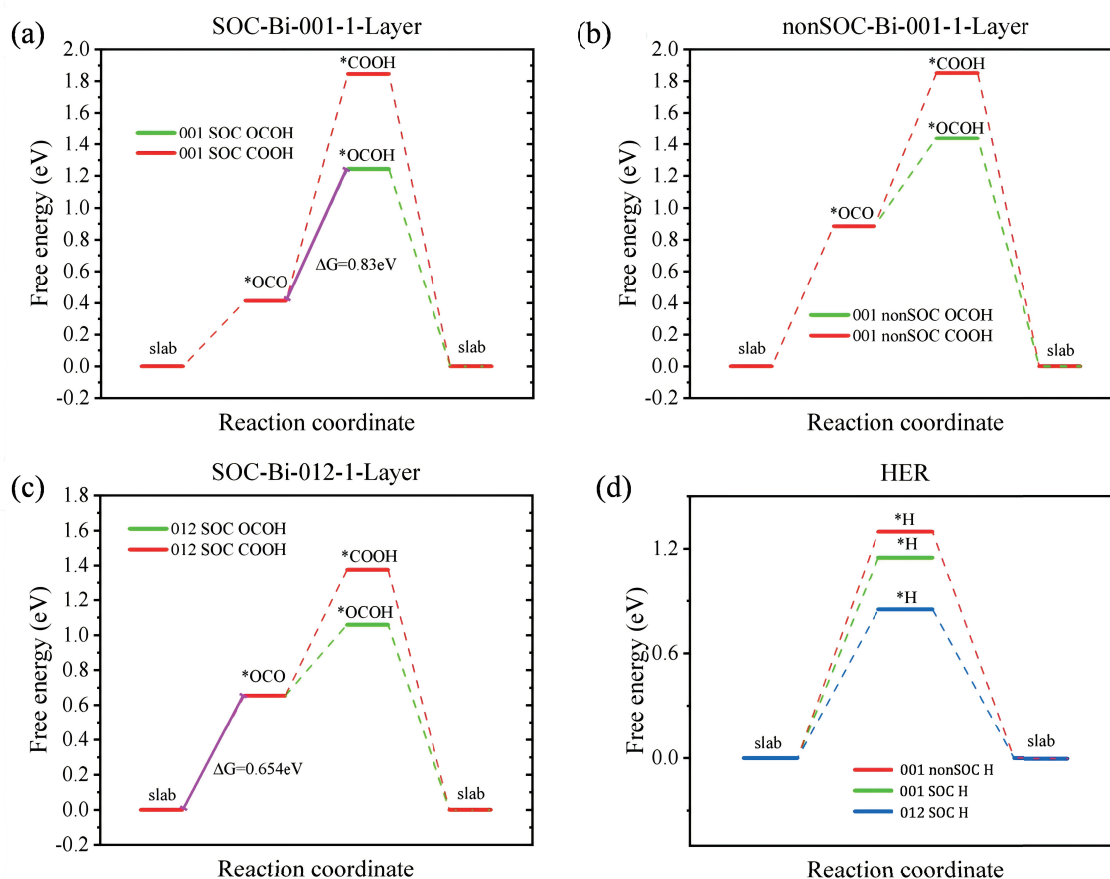| Absorb Structure	G/eV	ΔG/eV (U = 0 V)	ΔG/eV (U = 0.1655 V)
	Bi-SOC-012-1-Layer		
slab	−102.207	0.000	0.000
*OCO	−101.553	0.654	0.654
*OCOH	−100.983	1.224	1.059
*slab	−101.876	0.331	0.000
*COOH	−100.666	1.541	1.376

Figure 3. The Gibbs free energy change (ΔG) diagrams at U = 0.1655 V versus RHE are represented. (**a**,**b**) show the step diagrams of different CO_2RR pathways on Bi-001-1-Layer with and without SOC effect, respectively. (**c**) The step diagram of different CO_2RR pathways on Bi-012-1-Layer with SOC effect. (**d**) The step diagrams of HER on Bi-001-1-Layer with and without SOC effect, and the step diagrams of HER on Bi-012-1-Layer with SOC effect.

The ΔG free energies of *OCO, *OCOH, and *COOH on the Bi-001-1-Layer surface with SOC effect are 0.414 eV, 1.244 eV, and 1.846 eV and without SOC effect are 0.885 eV, 1.439 eV, and 1.851 eV, respectively, as shown in Table 1. These results show that the effect of SOC on the *COOH adsorption system is minimal, whereas its impact on *OCO and *OCOH are significant. As shown in Figure 2, *COOH adsorbs onto the catalyst surface via the C atom, whereas *OCO and *OCOH adsorb through the O atom. The O-Bi bond is highly sensitive to spin–orbit coupling. Bi, as a heavy element, exhibits a pronounced SOC effect, which is in accordance with our computational results.

Additionally, since CO_2RR typically occurs in formate solutions, HER becomes the primary competing reaction on the catalyst surface. The reaction free energies (G) of HER on different exposed surfaces of the Bi-1-Layer (vibrationally corrected) are shown in

Table 2. Considering the influence of SOC, the calculated adsorption free energies of *H on the Bi-001-1-Layer and Bi-012-1-Layer surfaces are 1.272 eV and 0.852 eV, respectively (see the green and blue dashed lines in Figure 3d). Both of them have larger energy barriers than the step of *OCO adsorption (0.414 and 0.654 eV) or the step of *OCO to *OCOH (0.830 and 0.590 eV) on the Bi-001-1-Layer and Bi-012-1-Layer surfaces, respectively. It is evident that CO_2RR holds a greater reaction advantage over HER on these catalysts. Therefore, CO_2RR is kinetically preferred over HER in the catalytic process.

Table 2. Reaction free energies (G) of HER on different exposed surfaces of Bi-1-Layer (vibrationally corrected).

Absorb Structure	G/eV	ΔG/eV
Bi-SOC-001-1-Layer		
slab	−144.041	0.000
*H	−142.770	1.272
*slab	−144.041	0.000
Bi-nonSOC-001-1-Layer		
slab	−125.126	0.000
*H	−123.828	1.298
*slab	−125.126	0.000
Bi-SOC-012-1-Layer		
slab	−79.001	0.000
*H	−78.149	0.852
*slab	−79.001	0.000

3.3. Calculation and Analysis of Energy Band of Intermediates in Bismuthene for CO_2RR

The electronic band structures of the Bi(001) surfaces without and with the adsorption of *OCOH, *H, and *COOH intermediates with SOC effect are plotted in Figure 4a–d, respectively. Our results show that there is a small gap in the electronic band structures of the one-layer Bi(001) surface at the $\tilde{\Gamma}$-point [see Figure 4a]. With the adsorption of *OCOH, *H, and *COOH intermediates, there are new states around the Fermi level, as shown in Figure 4b–d. From the projected electronic band structure of the Bi(001) surface with the adsorption of the *OCOH intermediate, we observe that the C and O orbitals contribute to the states near the Fermi level [see Figure 4b]. Similarly, for the Bi(001) surface with the adsorption of the *H intermediate, the H orbitals contribute to the states near the Fermi level [see Figure 4c]. From the projected electronic band structure of the Bi(001) surface with the adsorption of the *COOH intermediate, we find that the C orbitals contribute to the states near the Fermi level [see Figure 4d].

The electronic band structures of the Bi(012) surfaces without and with the adsorption of *OCOH, *H, and *COOH intermediates with SOC effect are also plotted in Figure 4e–h, respectively. The calculated results show that the one-layer Bi(012) surface is metallic [see Figure 4e]. From the projected electronic band structure of the Bi(012) surface with the adsorption of the *OCOH intermediate, we observe that the O orbitals contribute to the states near the Fermi level [see Figure 4f]. For the Bi(012) surface with the adsorption of the *H intermediate, the H orbitals make a minor contribution to the states near the Fermi level [see Figure 4g]. Also, for the Bi(012) surface with the adsorption of the *COOH intermediate, the C and O orbitals contribute to the states near the Fermi level [see Figure 4h]. Moreover, the adsorption of intermediates induces the splitting of electronic energy levels [see Figure 4]. These results indicate that different intermediates have distinct effects on the electronic properties of the systems. Specifically, on both the Bi(001) and Bi(012) surfaces,

the projected electronic band structure of the *OCOH intermediate at the Fermi level is significantly more pronounced compared to that of the *H and *COOH intermediates. This indicates that both the intermediate and the system are more active when *OCOH is adsorbed, which could explain the higher catalytic activity associated with the adsorption of the *OCOH intermediate [33,48].
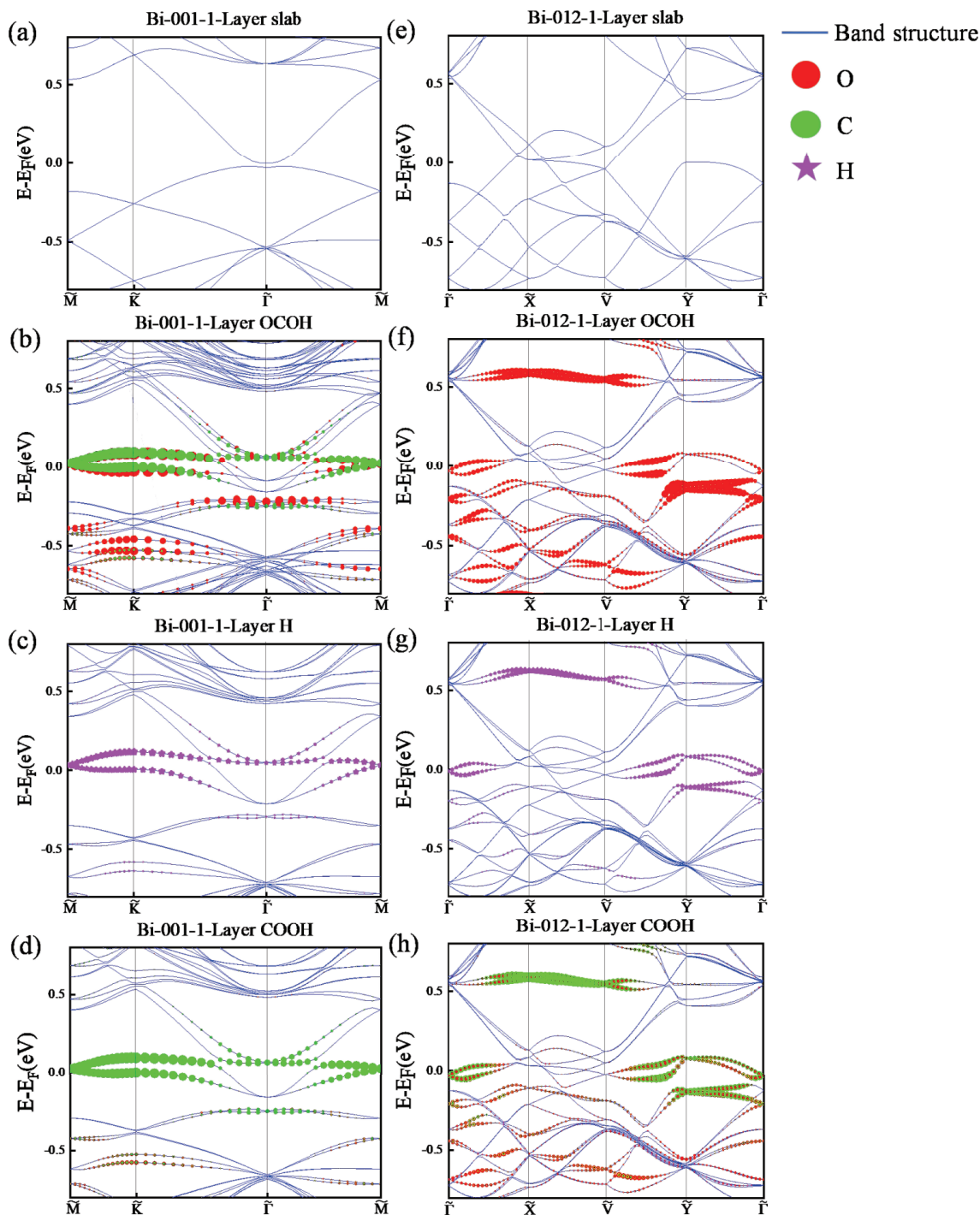

Figure 4. (**a–d**) The electronic band structures of the Bi(001) surface (**a**) without and with the adsorption of (**b**) *OCOH, (**c**) *H, and (**d**) *COOH intermediates with SOC effect, respectively. The high-symmetry points are M̃ (0.5, 0, 0), K̃ (0.333, 0.333, 0), and Γ̃ (0, 0, 0) in fractional coordinates. (**e–h**) The electronic band structures of the Bi(012) surface (**e**) without and with the adsorption of (**f**) *OCOH, (**g**) *H, and (**h**) *COOH intermediates with SOC effect, respectively. The high-symmetry points are Γ̃ (0, 0, 0), X̃ (0.5, 0, 0), Ṽ (0.5, 0.5, 0), and Ỹ (0, 0.5, 0) in fractional coordinates. The red, green, and purple dots represent the projections of O, C, and H orbitals, respectively.

4. Conclusions

In conclusion, this work investigates the 2D bismuthene catalysts of the Bi(001) and Bi(012) surfaces in the CO_2 reduction reaction through first-principles calculations. Surface energy calculations of monolayer and multilayer bismuthene confirmed that monolayer bismuthene is stable and suitable for catalytic applications on the Bi(001) surface. The adsorption free energy calculations suggest that both the Bi(001) and Bi(012) surfaces have high selectivity for the formation of *OCHO, leading to the fact that the catalytic products of CO_2RR on these substrates are formic acid. Furthermore, the rate-determining step (RDS) of CO_2RR on the (012) surface is the adsorption of *OCO with the ΔG of 0.654 eV. The RDS of the (001) surface is the reaction of *OCO to *OCOH with the ΔG of 0.830 eV. These results show the Bi(012) surface has a lower free-energy barrier than Bi(001) in the CO_2RR process, representing higher catalytic activity. The calculated adsorption free energies of *H on the Bi-001-1-Layer and Bi-012-1-Layer surfaces are 1.272 eV and 0.852 eV, respectively. Both of them have larger energy barriers than the step of *OCO adsorption or the step of *OCO to *OCOH on the Bi-001-1-Layer and Bi-012-1-Layer surfaces, respectively. It is evident that CO_2RR holds a greater reaction advantage over HER on these catalysts. By calculating the band structures of the Bi-001-1-Layer and Bi-012-1-Layer after the adsorption of various CO_2RR intermediates, it is shown that the different intermediates have effects on the electronic properties of the systems. These results provide theoretical insights for designing bismuthene-based CO_2RR catalysts with reduced overpotential (0.830 eV and 0.654 eV for Bi-001-1-layer and Bi-012-1-layer, respectively), enhanced selectivity, and improved electrocatalytic efficiency for formate (*OCOH) formation from CO_2 reduction and also offer useful guidance for carbon dioxide reduction on other metal surfaces.

Author Contributions: Conceptualization, C.-T.W.; Data Curation, Q.Y.; Funding Acquisition, Y.X. and C.Z.; Investigation, Q.Y.; Resources, C.W., Y.X., and C.Z.; Software, C.W., Y.X., and C.Z.; Writing— original draft, C.-T.W. and Q.Y.; Writing—review and editing, C.-T.W., C.W., Y.X., and C.Z. All authors have read and agreed to the published version of the manuscript.

Data Availability Statement: The original contributions presented in the study are included in the article, further inquiries can be directed to [ctwang@ustb.edu.cn].

Conflicts of Interest: The authors declare no conflicts of interest.

References

1. Novoselov, K.S.; Geim, A.K.; Morozov, S.V.; Jiang, D.; Zhang, Y.; Dubonos, S.V.; Grigorieva, I.V.; Firsov, A.A. Electric field effect in atomically thin carbon films. *Science* **2004**, *306*, 666–669. https://doi.org/10.1126/science.1102896.
2. Mayorov, A.S.; Gorbachev, R.V.; Morozov, S.V.; Britnell, L.; Jalil, R.; Ponomarenko, L.A.; Blake, P.; Novoselov, K.S.; Watanabe, K.; Taniguchi, T.; et al. Micrometer-Scale Ballistic Transport in Encapsulated Graphene at Room Temperature. *Nano Lett.* **2011**, *11*, 2396–2399. https://doi.org/10.1021/nl200758b.
3. Moore, J.E. The birth of topological insulators. *Nature* **2010**, *464*, 194–198. https://doi.org/10.1038/nature08916.
4. Schaibley, J.R.; Yu, H.Y.; Clark, G.; Rivera, P.; Ross, J.S.; Seyler, K.L.; Yao, W.; Xu, X.D. Valleytronics in 2D materials. *Nat. Rev. Mater.* **2016**, *1*, 16055. https://doi.org/10.1038/natrevmats.2016.55.
5. Wang, Q.H.; Kalantar-Zadeh, K.; Kis, A.; Coleman, J.N.; Strano, M.S. Electronics and optoelectronics of two-dimensional transition metal dichalcogenides. *Nat. Nanotechnol.* **2012**, *7*, 699–712. https://doi.org/10.1038/nnano.2012.193.
6. Chia, X.Y.; Pumera, M. Characteristics and performance of two-dimensional materials for electrocatalysis. *Nat. Catal.* **2018**, *1*, 909–921. https://doi.org/10.1038/s41929-018-0181-7.
7. Bellani, S.; Bartolotta, A.; Agresti, A.; Calogero, G.; Grancini, G.; Di Carlo, A.; Kymakis, E.; Bonaccorso, F. Solution-processed two-dimensional materials for next-generation photovoltaics. *Chem. Soc. Rev.* **2021**, *50*, 11870–11965. https://doi.org/10.1039/d1cs00106j.

8. Fu, X.B.; Pedersen, J.B.; Zhou, Y.Y.; Saccoccio, M.; Li, S.F.; Salinas, R.; Li, K.T.; Andersen, S.Z.; Xu, A.N.; Deissler, N.H.; et al. Continuous-flow electrosynthesis of ammonia by nitrogen reduction and hydrogen oxidation. *Science* **2023**, *379*, 707–712. https://doi.org/10.1126/science.adf4403.

9. Liu, Y.J.; Zhao, J.X.; Cai, Q.H. Pyrrolic-nitrogen doped graphene: A metal-free electrocatalyst with high efficiency and selectivity for the reduction of carbon dioxide to formic acid: A computational study. *Phys. Chem. Chem. Phys.* **2016**, *18*, 5491–5498. https://doi.org/10.1039/c5cp07458d.

10. Schindler, F.; Cook, A.M.; Vergniory, M.G.; Wang, Z.J.; Parkin, S.S.P.; Bernevig, B.A.; Neupert, T. Higher-order topological insulators. *Sci. Adv.* **2018**, *4*, eaat0346. https://doi.org/10.1126/sciadv.aat0346.

11. Yeom, H.W.; Jin, K.H.; Jhi, S.H. Topological fate of edge states of single Bi bilayer on Bi(111). *Phys. Rev. B* **2016**, *93*, 075435. https://doi.org/10.1103/PhysRevB.93.075435.

12. Xue, Y.; Guo, Y.; Cui, H.; Zhou, Z. Catalyst Design for Electrochemical Reduction of CO_2 to Multicarbon Products. *Small Methods* **2021**, *5*, 2100736. https://doi.org/10.1002/smtd.202100736.

13. Liang, S.; Altaf, N.; Huang, L.; Gao, Y.; Wang, Q. Electrolytic cell design for electrochemical CO_2 reduction. *J. CO_2 Util.* **2020**, *35*, 90–105. https://doi.org/10.1016/j.jcou.2019.09.007.

14. Chen, Q.; Wang, X.; Zhou, Y.; Tan, Y.; Li, H.; Fu, J.; Liu, M. Electrocatalytic CO_2 Reduction to C2+ Products in Flow Cells. *Adv. Mater.* **2024**, *36*, 2303902. https://doi.org/10.1002/adma.202303902.

15. Huo, S.; Weng, Z.; Wu, Z.; Zhong, Y.; Wu, Y.; Fang, J.; Wang, H. Coupled Metal/Oxide Catalysts with Tunable Product Selectivity for Electrocatalytic CO_2 Reduction. *ACS Appl. Mater. Interfaces* **2017**, *9*, 28519–28526. https://doi.org/10.1021/acsami.7b07707.

16. Guo, J.; Zhi, X.; Wang, D.; Qu, L.; Zavabeti, A.; Fan, Q.; Zhang, Y.; Butson, J.D.; Yang, J.; Wu, C.; et al. Surface-Enriched Room-Temperature Liquid Bismuth for Catalytic CO2 Reduction. *Small* **2024**, *20*, 2401777. https://doi.org/10.1002/smll.202401777.

17. Cho, W.S.; Hong, D.M.; Dong, W.J.; Lee, T.H.; Yoo, C.J.; Lee, D.; Jang, H.W.; Lee, J.-L. Porously Reduced 2-Dimensional BiOCO Petals for Strain-Mediated Electrochemical CO Reduction to HCOOH. *Energy Environ. Mater.* **2024**, *7*, e12490. https://doi.org/10.1002/eem2.12490.

18. Kaiyue, H.; Jiayu, T.; Zhifu, Z.; Daming, Z.; Xiangjiu, G. Direct Z-scheme photocatalytic systems based on vdW heterostructures for water splitting and CO_2 reduction: Fundamentals and recent advances. *Microstructures* **2024**, *4*, 2024021. https://doi.org/10.20517/microstructures.2023.76.

19. Masoumi, Z.; Tayebi, M.; Tayebi, M.; Masoumi Lari, S.A.; Sewwandi, N.; Seo, B.; Lim, C.-S.; Kim, H.-G.; Kyung, D. Electrocatalytic Reactions for Converting CO_2 to Value-Added Products: Recent Progress and Emerging Trends. *Int. J. Mol. Sci.* **2023**, *24*, 9952. https://doi.org/10.3390/ijms24129952.

20. Chattopadhyay, S.; Cheah, M.H.; Lomoth, R.; Hammarström, L. Direct Detection of Key Intermediates during the Product Release in Rhenium Bipyridine-Catalyzed CO_2 Reduction Reaction. *ACS Catal.* **2024**, *14*, 16324–16334. https://doi.org/10.1021/acscatal.4c06044.

21. Lee, J.; Lim, J.; Roh, C.W.; Whang, H.S.; Lee, H. Electrochemical CO_2 reduction using alkaline membrane electrode assembly on various metal electrodes. *J. CO_2 Util.* **2019**, *31*, 244–250. https://doi.org/10.1016/j.jcou.2019.03.022.

22. Huang, Z.; Grim, R.G.; Schaidle, J.A.; Tao, L. The economic outlook for converting CO_2 and electrons to molecules. *Energy Environ. Sci.* **2021**, *14*, 3664–3678. https://doi.org/10.1039/d0ee03525d.

23. Cao, B.; Li, F.-Z.; Gu, J. Designing Cu-Based Tandem Catalysts for CO2 Electroreduction Based on Mass Transport of CO Intermediate. *ACS Catal.* **2022**, *12*, 9735–9752. https://doi.org/10.1021/acscatal.2c02579.

24. Sliwa, M.; Zhang, H.; Gao, J.X.; Stephens, B.O.; Patera, A.J.; Raciti, D.; Hanrahan, P.D.; Warecki, Z.A.; Foley, D.L.; Livi, K.J.; et al. Selective CO_2 Reduction Electrocatalysis Using AgCu Nanoalloys Prepared by a "Host-Guest" Method. *Nano Lett.* **2024**, *24*, 13911–13918. https://doi.org/10.1021/acs.nanolett.4c02638.

25. Sun, H.H.; Wang, M.X.; Zhu, F.F.; Wang, G.Y.; Ma, H.Y.; Xu, Z.A.; Liao, Q.; Lu, Y.H.; Gao, C.L.; Li, Y.Y.; et al. Coexistence of Topological Edge State and Superconductivity in Bismuth Ultrathin Film. *Nano Lett.* **2017**, *17*, 3035–3039. https://doi.org/10.1021/acs.nanolett.7b00365.

26. Han, N.; Wang, Y.; Yang, H.; Deng, J.; Wu, J.H.; Li, Y.F.; Li, Y.G. Ultrathin bismuth nanosheets from in situ topotactic transformation for selective electrocatalytic CO_2 reduction to formate. *Nat. Commun.* **2018**, *9*, 1320. https://doi.org/10.1038/s41467-018-03712-z.

27. Yang, H.; Han, N.; Deng, J.; Wu, J.H.; Wang, Y.; Hu, Y.P.; Ding, P.; Li, Y.F.; Li, Y.G.; Lu, J. Selective CO_2 Reduction on 2D Mesoporous Bi Nanosheets. *Adv. Energy Mater.* **2018**, *8*, 1801536. https://doi.org/10.1002/aenm.201801536.

28. Cao, C.S.; Ma, D.D.; Gu, J.F.; Xie, X.Y.; Zeng, G.; Li, X.F.; Han, S.G.; Zhu, Q.L.; Wu, X.T.; Xu, Q. Metal-Organic Layers Leading to Atomically Thin Bismuthene for Efficient Carbon Dioxide Electroreduction to Liquid Fuel. *Angew. Chem. Int. Ed.* **2020**, *59*, 15014–15020. https://doi.org/10.1002/anie.202005577.

29. Fan, J.; Zhao, X.; Mao, X.N.; Xu, J.; Han, N.; Yang, H.; Pan, B.B.; Li, Y.S.; Wang, L.; Li, Y.G. Large-Area Vertically Aligned Bismuthene Nanosheet Arrays from Galvanic Replacement Reaction for Efficient Electrochemical CO_2 Conversion. *Adv. Mater.* **2021**, *33*, 2100910. https://doi.org/10.1002/adma.202100910.

30. Li, Y.X.; Hui, D.P.; Sun, Y.Q.; Wang, Y.; Wu, Z.J.; Wang, C.Y.; Zhao, J.C. Boosting thermo-photocatalytic CO_2 conversion activity by using photosynthesis-inspired electron-proton-transfer mediators. *Nat. Commun.* **2021**, *12*, 123. https://doi.org/10.1038/s41467-020-20444-1.

31. Ma, W.X.; Bu, J.; Liu, Z.P.; Yan, C.; Yao, Y.; Chang, N.H.; Zhang, H.P.; Wang, T.; Zhang, J. Monoclinic Scheelite Bismuth Vanadate Derived Bismuthene Nanosheets with Rapid Kinetics for Electrochemically Reducing Carbon Dioxide to Formate. *Adv. Funct. Mater.* **2021**, *31*, 2006704. https://doi.org/10.1002/adfm.202006704.

32. Yang, J.; Wang, X.L.; Qu, Y.T.; Wang, X.; Huo, H.; Fan, Q.K.; Wang, J.; Yang, L.M.; Wu, Y.E. Bi-Based Metal-Organic Framework Derived Leafy Bismuth Nanosheets for Carbon Dioxide Electroreduction. *Adv. Energy Mater.* **2020**, *10*, 2001709. https://doi.org/10.1002/aenm.202001709.

33. Yang, F.; Elnabawy, A.O.; Schimmenti, R.; Song, P.; Wang, J.W.; Peng, Z.Q.; Yao, S.; Deng, R.P.; Song, S.Y.; Lin, Y.; et al. Bismuthene for highly efficient carbon dioxide electroreduction reaction. *Nat. Commun.* **2020**, *11*, 1088. https://doi.org/10.1038/s41467-020-14914-9.

34. Siinor, L.; Lust, K.; Lust, E. Impedance study of adsorption of iodide ions at Bi(001) electrode from the aqueous solutions with constant ionic strength. *J. Electroanal. Chem.* **2007**, *601*, 39–46. https://doi.org/10.1016/j.jelechem.2006.10.031.

35. Wang, J.-Z.; Lan, M.; Shao, T.-N.; Li, G.-Q.; Zhang, Y.; Huang, C.-Z.; Xiong, Z.-H.; Ma, X.-C.; Jia, J.-F.; Xue, Q.-K. STM study of a rubrene monolayer on Bi(001): Structural modulations. *Phys. Rev. B* **2011**, *83*, 235433. https://doi.org/10.1103/PhysRevB.83.235433.

36. Bychkov, Y.A.; Rashba, E.I. Oscillatory Effects and the Magnetic-Susceptibility of Carriers in Inversion-Layers. *J. Phys. C Solid State Phys.* **1984**, *17*, 6039–6045. https://doi.org/10.1088/0022-3719/17/33/015.

37. Kresse, G.; Furthmüller, J. Efficiency of ab-initio total energy calculations for metals and semiconductors using a plane-wave basis set. *Comput. Mater. Sci.* **1996**, *6*, 15–50. https://doi.org/10.1016/0927-0256(96)00008-0.

38. Kresse, G.; Furthmuller, J. Efficient iterative schemes for ab initio total-energy calculations using a plane-wave basis set. *Phys. Rev. B* **1996**, *54*, 11169–11186. https://doi.org/10.1103/PhysRevB.54.11169.

39. Blochl, P.E. Projector Augmented-Wave Method. *Phys. Rev. B* **1994**, *50*, 17953–17979. https://doi.org/10.1103/PhysRevB.50.17953.

40. Kresse, G.; Joubert, D. From ultrasoft pseudopotentials to the projector augmented-wave method. *Phys. Rev. B* **1999**, *59*, 1758–1775. https://doi.org/10.1103/PhysRevB.59.1758.

41. Perdew, J.P.; Burke, K.; Wang, Y. Generalized gradient approximation for the exchange-correlation hole of a many-electron system. *Phys. Rev. B* **1996**, *54*, 16533–16539. https://doi.org/10.1103/PhysRevB.54.16533.

42. Perdew, J.P.; Burke, K.; Ernzerhof, M. Generalized gradient approximation made simple. *Phys. Rev. Lett.* **1996**, *77*, 3865–3868. https://doi.org/10.1103/PhysRevLett.77.3865.

43. Klimes, J.; Bowler, D.R.; Michaelides, A. Chemical accuracy for the van der Waals density functional. *J. Phys. Condens. Matter* **2010**, *22*, 022201. https://doi.org/10.1088/0953-8984/22/2/022201.

44. Klimes, J.; Bowler, D.R.; Michaelides, A. Van der Waals density functionals applied to solids. *Phys. Rev. B* **2011**, *83*, 195131. https://doi.org/10.1103/PhysRevB.83.195131.

45. Reis, F.; Li, G.; Dudy, L.; Bauernfeind, M.; Glass, S.; Hanke, W.; Thomale, R.; Schäfer, J.; Claessen, R. Bismuthene on a SiC substrate: A candidate for a high-temperature quantum spin Hall material. *Science* **2017**, *357*, 287–290. https://doi.org/10.1126/science.aai8142.

46. Zhang, Y.; Zhang, X.L.; Ling, Y.Z.; Li, F.W.; Bond, A.M.; Zhang, J. Controllable Synthesis of Few-Layer Bismuth Subcarbonate by Electrochemical Exfoliation for Enhanced CO_2 Reduction Performance. *Angew. Chem. Int. Ed.* **2018**, *57*, 13283–13287. https://doi.org/10.1002/anie.201807466.

47. Available online: https://webbook.nist.gov/chemistry/ (accessed on 1 January 2023).

48. Xu, A.; Wei, D.; Chen, X.; Yang, T.; Huang, Y.; He, H.; Xu, J. In situ transformation of bismuth-containing precursors into ultrathin bismuth nanosheets for enhanced electrochemical CO_2 reduction. *Chem. Eng. J.* **2023**, *452*, 139227. https://doi.org/10.1016/j.cej.2022.139227.